NUMERICAL SIMULATION OF WIND-AIDED FLAME SPREAD OVER HORIZONTAL SURFACE OF CONDENSED FUEL IN A CONFINED CHANNEL

H.Y. Wang and B. Chateil
Laboratoire de Combustion et de Détonique, C.N.R.S. UPR 9028 - E.N.S.M.A., Université de Poitiers
BP 109 - Site du Futuroscope, 86960, Futuroscope Cedex, France

(Received 26 February 2008; Accepted 8 May 2008)

ABSTRACT

Numerical study is performed to investigate flame spread and burning over horizontal polymethylmethacrylate (PMMA, $C_5H_8O_2$) surface exposed to air cross-flow with a velocity ranging from 0.5 to 2.5 ms^{-1} in a confined channel. Controlling mechanisms of three dimensional flow, combustion, soot formation and radiation are coupled with a Large Eddy Simulation. The computed, time-averaged flame shape (length/height) and heat flux are compared with experimental data from a gas burner fire in a model channel, and a relatively good agreement is attained. The numerical results suggest that the flame propagation in large scale over condensed fuel surface occurs in two successive modes. In the first mode, when the flame is confined within a boundary layer, the flame spread rate increases slowly with the pyrolysis front. Transition to the second mode, occurring earlier at wind velocity lower than 1 ms^{-1} when the flame stands up into a plume, the flame spread is strongly accelerated up to an asymptotic value of 3 ± 0.5 cms^{-1}. The burning rate of the condensed fuel increases with the pyrolysis front during fire propagation, reaching finally the maximum burning rate of 28 $gm^{-2}s^{-1}$ for PMMA. With an increase of the wind velocity, an increase of the convection flux is accompanied by a reduction in the radiation flux, leading to a total heat flux practically independent to the wind velocity. It is found that the flame shape (length/height) is strongly controlled by the ventilation conditions, called as fuel or ventilation controlled fire. The flame length is approximately 2 times the pyrolysis length for the fuel controlled fire ($U_0 > 1.5$ ms^{-1}), and up to 4 times the pyrolysis length for the ventilation controlled fire.

1. INTRODUCTION

The phenomenological analysis of wind-assisted flame spread has been made to gain insight into the mechanisms governing the flame propagation. The flame shape is first described mainly from sets of equations derived by applying Froude or Grashof/Reynolds numbers preservation, combined with their experimental data [1,2]. In order to avoid the coupling between the heat transfer and flame propagation, the wind-assisted fire propagation is experimentally studied [3,4] by using a horizontal model tunnel with propane gas burner as fire sources. Since task of obtaining enough experimental data is still very difficult to describe how a wind-aided turbulent fire is evolved spatially and temporally inside a channel, the buoyancy effects in turbulent reacting flow have been the subject of many investigations [5,6] by numerical simulations. It was found that the buoyancy-related modifications in the standard $k-\varepsilon$ turbulence model strongly affected the extent of upstream propagation of the backlayering against the ventilation. Concerning the flame spread in large-scale over surface of a condensed fuel, modeling or theoretical treatments are significantly simplified through some assumptions. The flame spread rate is measured, and the flame-to-fuel surface heat fluxes are estimated from the existing flame spread theories [7]. A semi-empirical results derived for a turbulent wind-aided spread show that the flame length is only a function of the pyrolysis length [7]. By assuming that convective heat transfer can be neglected, a flame spread correlation over horizontal PMMA surface is developed [8]. In the other study [9], the experimental study indicates that for a flat plate boundary layer flow, radiation from the flame to the solid fuel (PMMA) has a secondary role, and the mass burning rate is only in terms of convective heat transfer parameter. However, a rigorous study must resort to large-scale fires for validating their assumptions.

This work has focused on a rigorous analysis of turbulent wind-aided flame spread over surface of a condensed fuel in a confined channel on a scale where both radiation and buoyancy are significant. Large Eddy Simulation (LES) is used for resolving the instantaneous position of the highly oscillating, buoyancy controlled, three-dimensional and elliptic reacting flow. A soot formation/oxidation model and wall function are implemented within the Fire Dynamics Simulation (FDS) code [10]. This approach to the field modeling of fire spread over condensed fuel surface includes the material properties, heat transfer to the fuel, chemical kinetics, soot and turbulence effects. The time-

averaged flame height/length, and flame-surface heat flux are compared with the experimental data [3] based on a wind-assisted gas burner fire, and a relatively good agreement is obtained. Then, predictions are provided of the transient mass loss, heat flux and flame shape (length/height) with the pyrolysis front during the flame propagation at various wind velocities.

2. THEORETICAL ANALYSIS

The starting point of the analysis is the set of the continuity equation, the three momentum equations in each of the three space dimensions, the equation for conservation of chemical species, of the soot, and radiative transfer equation.

2.1 Flowfield Model

LES is based on a filtering operation, which decomposes a full flowfield, $\varphi(x,t)$, into a resolved component, $\overline{\varphi}(x,t)$, and a SubGrid-Scale (SGS) component, $\varphi'(x,t)$. Applying the filtering operation to each term in the conservation equations of mass, momentum, energy and species, and decomposing the dependent variables (u, v, w, p, etc.) into resolved and subgrid components results in the filtered governing equations, shown below:

$$\frac{\partial \rho}{\partial t}+\frac{\partial \rho \overline{u}_j}{\partial x_j}=0 \tag{1}$$

$$\frac{\partial \rho \overline{u}_i}{\partial t}+\frac{\partial (\rho \overline{u}_i \overline{u}_j)}{\partial x_j}+\frac{\partial \overline{p}}{\partial x_i}-\rho g_i=\nabla \cdot \overline{\tau}_{ij,SGS} \tag{2}$$

where an overbar denotes the filtered variable. The unresolved field, $\varphi'(x,t)$, is modeled by the Smagorinsky model [11]. The SGS Reynolds stresses tensor, $\overline{\tau}_{ij,SGS}$, are related to the local large scale rate of strain.

$$\overline{\tau}_{ij,SGS}=2\mu_t \overline{S}_{ij} \text{ and } \overline{S}_{ij}=\frac{1}{2}\left(\frac{\partial \overline{u}_i}{\partial x_j}+\frac{\partial \overline{u}_j}{\partial x_i}\right) \tag{3}$$

Following the analysis of Smagorinsky [11], the eddy viscosity can be modelled as:

$$\mu_t=C_s^2 \rho \Delta^2 \left|\overline{S}_{ij}\right| \tag{4}$$

Here, $\left|\overline{S}_{ij}\right|$ is the magnitude of the large scale strain rate tensor, $\overline{S}_{ij}$, $\Delta=(\Delta x \Delta y \Delta z)^{1/3}$ the filter width, and C_s an empirical constant with a standard value of 0.21. The turbulent heat flux is based on an eddy viscosity assumption, resulting in the following energy equation:

$$\frac{\partial \rho \overline{h}}{\partial t}+\frac{\partial (\rho \overline{u}_i \overline{h})}{\partial x_j}-\frac{\partial}{\partial x_j}\left(\frac{\mu_t}{\mathrm{Pr}_t}\frac{\partial \overline{h}}{\partial x_j}\right)=\dot{q}_c'''-\nabla \cdot q_r \tag{5}$$

where Pr_t denotes the turbulent Prandtl number with $\mathrm{Pr}_t = 1$. The energy equation includes the rate of heat release per unit volume, $\dot{q}_c'''$, and the radiant energy flux, $-\nabla \cdot \mathbf{q}_r$. Finally, the perfect gas law is used to describe the equation of state.

2.2 Combustion Model

A global one-step irreversible chemical reaction for complete combustion of PMMA is assumed.

$$C_5H_8O_2 + 6\ O_2 \rightarrow 5\ CO_2 + 4H_2O \tag{6}$$

The amount of energy released from this chemical reaction per unit mass of PMMA consumed is about 25200 $kJkg^{-1}$. Based on the infinitely fast-chemistry assumption of Schvab-Zeldovich formulation, the combustion processes are governed by the conservation equation for the filtered mixture fraction.

$$\frac{\partial \rho \overline{Z}}{\partial t}+\frac{\partial (\rho \overline{u}_i \overline{Z})}{\partial x_j}=\frac{\partial}{\partial x_j}\left(\frac{\mu_t}{Sc_t}\frac{\partial \overline{Z}}{\partial x_j}\right) \tag{7}$$

Here, Sc_t denotes the turbulent Schmit number with $Sc_t = 1$. From the thin flame sheet concept, a linear state relation between the mass fraction of chemical species, Y_i (i = fuel, O_2, CO_2 and H_2O), and mixture fraction, Z, can be esthablished, as shown in Fig. 1. Multiplying the constant, $dY_0(Z)/dZ$, to each term in equation (7) results in the following equation:

$$\frac{\partial \rho \overline{Z}}{\partial t}\frac{dY_o}{dZ}+\frac{\partial (\rho \overline{u}_i \overline{Z})}{\partial x_j}\frac{dY_o}{dZ}=\frac{\partial}{\partial x_j}\left(\frac{\mu_t}{Sc_t}\frac{\partial \overline{Z}}{\partial x_j}\right)\frac{dY_o}{dZ} \tag{8}$$

The oxygen mass conservation equation is given as:

$$\frac{\partial \rho \overline{Y}_O}{\partial t}+\frac{\partial (\rho \overline{u}_i \overline{Y}_O)}{\partial x_j}=\frac{\partial}{\partial x_j}\left(\frac{\mu_t}{Sc_t}\frac{\partial \overline{Y}_O}{\partial x_j}\right)+\dot{\omega}_O \tag{9}$$

By combining the two conservation equations of the mixture fraction, equation (8), and oxygen mass fraction, equation (9), and after a mathematical arrangement, an expression for the rate of oxygen mass consumption can be derived.

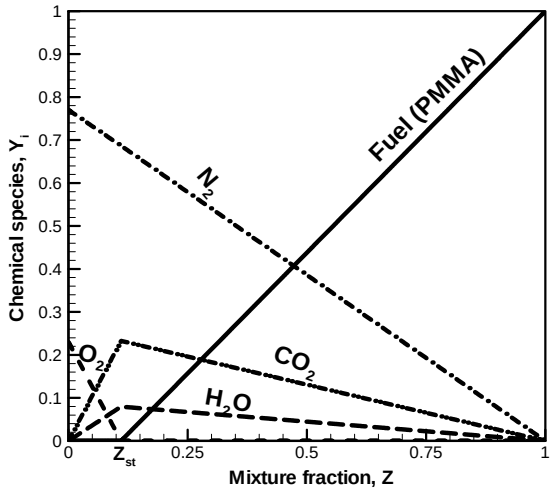

Fig. 1: Relation between chemical species (fuel, O_2, CO_2 and H_2O) and the mixture fraction, Z

$$-\dot{\omega}_o = \frac{\partial}{\partial x_j}\left(\frac{\mu_t}{Sc_t}\frac{dY_o(Z)}{dZ}\frac{\partial \bar{Z}}{\partial x_j}\right) - \frac{dY_o(Z)}{dZ}\frac{\partial}{\partial x_j}\left(\frac{\mu_t}{Sc_t}\frac{\partial \bar{Z}}{\partial x_j}\right) = \frac{\mu_t}{Sc_t}\frac{d^2Y_o(Z)}{dZ^2}\left|\nabla \bar{Z}\right|^2 \quad (10)$$

Neither of these expressions in equation (10) for the local oxygen consumption rate is particularly convenient to apply numerically because of the discontinuity of the derivative of Yo(Z) at stoichiometric ratio, Z = Z_{st} from state relation. However, an expression for the oxygen consumption rate per unit area of flame sheet can be derived from equation (10)

$$-\dot{\omega}_o = \left.\frac{dY_O(Z)}{dZ}\right|_{Z<Z_{st}} \frac{\mu_t}{Sc_t}\nabla \bar{Z}\cdot \boldsymbol{n} \quad (11)$$

where the term, $dY_0(Z)/dZ$, is derived from the state relation (cf. Fig. 1) and $\bar{Z}$ using the conservation equation for the mixture fraction, equation (7). In the numerical algorithm, the local heat release rate is computed by first locating the flame sheet, then computing the local heat release rate per unit area, and finally distributing this energy to the grid cells cut by the flame sheet. In this way, the ideal, infinitesimally thin flame sheet is smeared out over the width of a grid cell, consistent with all other gas phase quantities. Finally, the heat release rate is directly proportional to the rate of consumption of the available oxygen [12] controlled by the ventilation conditions:

$$\dot{q}_c''' = -H_o\dot{\omega}_o \quad (12)$$

Here, H_o is the amount of energy released per unit mass of oxygen consumed with a value of 13100 $kJkg^{-1}$. It should be noted that, in most fires, the primary momentum transport and turbulent diffusion is sustained by large-scale energy-containing eddies, and combustion processes can be crudely accounted for by this type model.

2.3 Soot Formation and Its Oxidation

In a heavily sooting flame, soot particles generated from combustion processes have a significant impact on the radiative heat transfer characteristics, and consequently, the flame spread rate. Up to now, coupling between LES and the detail chemistry to track the soot development stages in relation to its formation and destruction is not available due to the prohibitive computation cost for large-scale fire simulation. In this work, the soot formation and its oxidation are incorporated into a turbulent flow calculation in two convection-diffusion equations for the precursor particle density, n, and soot concentration, c_s. This model assumes that soot is formed from a gaseous fuel in two stages, where the first stage represents the formation of radical nuclei, and the second stage represents soot particle formation from these nuclei. Based on the kinetic theory of soot formation proposed by Tesner et al. [13], the rate of formation of the radical nuclei, n, is expressed by:

$$\frac{\partial \rho \bar{n}}{\partial t} + \frac{\partial(\rho \bar{u}_i \bar{n})}{\partial x_j} - \frac{\partial}{\partial x_j}\left(\frac{\mu_t}{Sc_t}\frac{\partial \bar{n}}{\partial x_j}\right) = A_0\rho\bar{Y}_F \exp(-E/R\bar{T}) + (f-g)\bar{n} - g_0\bar{n}\bar{N} - \bar{n}\dot{\omega}_{Oxid} \quad (13)$$

where f (s^{-1}) and g (s^{-1}) are branching and termination coefficients, and $\bar{N}$ (part m^{-3}) is the number density of soot particles. A_0 (s^{-1}) and E are the pre-exponential constant and activation energy, respectively. The rate of soot formation is given by:

$$\frac{\partial \rho \bar{c}_s}{\partial t} + \frac{\partial(\rho \bar{u}_i \bar{c}_s)}{\partial x_j} - \frac{\partial}{\partial x_j}\left(\frac{\mu_t}{Sc_t}\frac{\partial \bar{c}_s}{\partial x_j}\right) = m_p(\alpha - \beta\bar{N})\bar{n} - \bar{c}_s\dot{\omega}_{Oxid} \quad (14)$$

where α ($part^{-1}s^{-1}$) and β ($m^3part^{-2}s^{-1}$) are constants. The mass of a soot particle, m_p, is determined from its diameter and soot density as,

$$m_p = \frac{1}{6}\pi d_p^3 \rho_{soot} \quad (15)$$

The soot density, ρ_{soot}, is assumed to be 1800 kgm^{-3}. The Tesner et al. model [13] does not include a term for soot oxidation due to O_2. In this work, we have modified the Tesner et al. model by including an additional term for soot oxidation by using an Eddy-Break-Up (EBU) approach, allowing for taking into account the interaction

between soot oxidation and subgrid scale eddy motion.

$$\dot{\omega}_{Oxid} = C_{Ebu}\rho\frac{\varepsilon}{k}\min\left(1, \frac{\rho\bar{Y}_O}{\bar{c}_s\nu_s + \rho\bar{Y}_F\nu_F}\right) \quad (16)$$

This additional oxidation term results in lower soot volume fraction, especially for the turbulent diffusion flame. In equation (16), ν_s and ν_F are the stoichiometric oxygen requirements to burn 1 kg soot and fuel, respectively. C_{Ebu} is an empirical constant in EBU approach with a standard value of 4. The SGS kinetic energy and its dissipation are derived from the eddy viscosity and the filter width.

$$k = \left(\frac{\mu_t}{C_\mu\rho\Delta}\right)^2, \ \varepsilon = C_\varepsilon\frac{k^{3/2}}{\Delta} \quad (17)$$

Here, the empirical constants C_μ and C_ε are given as 0.0856 and 0.845, respectively. This model represents the rationale approach to soot treatment in the case where the exact chemical compositions of the PMMA are unlikely to be known. Various detailed soot formation models [14] would require accurate knowledge of fuel composition (methane, propane). Besides, even those models are not free from empirical parameters for the solid combustible, such as PMMA. In this type soot model, soot formation/oxidation has no effect on the scalar mixture fraction conservation equation. This approximation results in a uncertainty of about 2% in the numerical simulation.

2.4 Radiation Model

The radiation intensity, I, is found by solving the radiative transfer equation without scattering,

$$\vec{\nabla}.\vec{\Omega}I + \kappa I = \kappa\frac{\sigma\bar{T}^4}{\pi} \quad (18)$$

This equation is solved through the use of a Finite Volume Method described in Ref. [10]. Finally, the radiative source term in the energy equation is calculated from a discrete expression for the divergence of the radiative flux.

$$-\nabla\cdot\mathbf{q}_r = -\int_{4\pi}\vec{\nabla}.\vec{\Omega}I.d\Omega \approx \kappa(\sum_{l=1}^{L} w^l I^l - 4\sigma\bar{T}^4) \quad (19)$$

Here, w^l is weighting factor and σ Stefan-Boltzmann constant. For situations where the condensed fuel is a diffusively reflecting and emitting surface, the radiative boundary condition is given by:

$$I(r_w,\Omega) = \frac{\varepsilon_w\sigma T_w^4}{\pi} + \frac{1-\varepsilon_w}{\pi}\int_{n.\Omega}|n.\Omega'|I(r_w,\Omega')d\Omega' \quad (20)$$

The soot volume fraction, f_v, is obtained at any location from the soot number density, $\bar{N}$.

$$f_v = \frac{1}{6}\pi d_p^3\bar{N} \quad (21)$$

where the soot number density, $\bar{N}$, is derived from the soot concentration (equation 14) and the mass of a soot particle (equation 15),

$$\bar{N} = \bar{C}_s / m_p \quad (22)$$

By assuming soot particles to be spherical with a sufficiently small uniform diameter, d_p, of $0.02\ \mu m$, the particle temperature is locked closely to the local gas temperature, resulting in a radiative transfer without scattering. Moreover, the choice of this soot diameter is based on a good agreement between the predicted and measured radiation flux for the large-scale PMMA burning [15]. The overall absorption coefficient, κ, for the soot and gas (CO_2 and H_2O) mixture is calculated from a pseudo grey gas approximation through Modak model [16] in function of the temperature and concentration of combustion products.

2.5 Pyrolysis Model

In this study, the condensed fuel is assumed to be thermally-thin, that is, its temperature is assumed uniform across its thickness, $T_s(t)$ is affected by gains and losses due to convection, radiation and pyrolysis. The thermal lag of the material is a function of the product of its density, ρ_s, specific heat, c_s, and thickness δ.

$$\rho_s c_s\delta\frac{dT_s}{dt} = \dot{q}_{conv} + \dot{q}_{rad} - \dot{q}_{pyro} \quad (23)$$

Here, $\dot{q}_{pyro}$ is energy available for pyrolyzing the condensed fuel,

$$\dot{m}_s = \frac{\dot{q}_{pyro}}{h_g} \quad (24)$$

where $\dot{m}_s$ is the mass loss rate, and h_g the heat of vaporization of the condensed fuel. Flame radiation flux, $\dot{q}_{rad}$, is computed from a discrete representation of the radiative intensity equation (18). The Couette flow is assumed to prevail near the wall surface, and the convective heat feedback is calculated from a wall function [17],

$$\dot{q}_{conv} = \frac{(T_g - T_w)\rho c_p C_\mu^{1/4} k^{1/2}}{\Pr\left[\frac{1}{\kappa}\ln(E y^+) + P\right]} \quad (25)$$

far away from the wall for viscous effects to be negligible, that is, at $y^+ \geq 11$. The symbols are defined by Djilali et al. [17].

2.6 Method of Resolution

The finite-difference technique is used to discretize the partial differential equations. This procedure entails the subdividing of the calculation domain into a finite number of cells. The velocities (u_i) are taken on the boundary of each cell; and all the scalar variables are taken at cell centers. This staggered grid leads to a very efficient differencing scheme for the equations. All spatial derivatives are approximated by second-order central differences and the flow variables are updated in time using an explicit second-order Runge-Kutta scheme. The pressure is found by taking the divergence of the momentum equations, yielding a Poisson equation which is solved with an efficient flow solving technique [10]. The inert solid surface is considered as adiabatic, and the no-slip condition is imposed by setting all velocities to zero. The burning surface is considered as a pure combustible material, and the normal velocity is derived from the mass loss rate. The operation of software FDS is based on a single input text file containing parameters organized namelist groups. The input file provides FDS with all of the necessary information (grid, boundary conditions, material properties, etc) to describe the mechanisms governing the flame propagation. The input file is saved with a given name that helps to identify the simulation.

3. RESULTS AND DISCUSSION

The situation encountered in the present work is shown in Fig. 2a & b, where the PMMA with a length of L_p = 1 m, is mounted on a horizontal plate with a length, L, of 6 m in the x direction and a width, W, of 0.4 m in the transversal direction, y. The height, H, of the channel is 0.7 m, and thus, the magnitude of the PMMA length and channel height is almost identical. The PMMA is considered as thermally thin sheet with a constant thickness of 3 mm during flame propagation, and ignition temperature of 380°C [18] and emissivity of 1 are selected. The material (PMMA) properties used in the simulations take the following values [18]: h_g = 1620 kJkg^{-1}, ρ_s =1190 kgm^{-3} and c_s=1.42 kJkg^{-1}K^{-1} The upstream edge of the PMMA is ignited by a gas burner fire as shown in Fig. 2a, and the heat flux from the hotter gas of the combustion products incident upon the unburned fuel surface is responsible for a self-sustaining fire spreading concurrently with the wind, as illustrated in Fig. 2b. The wind is blowing at a mean velocity, U_0, varying from 0.5 to 2.5 ms^{-1}.

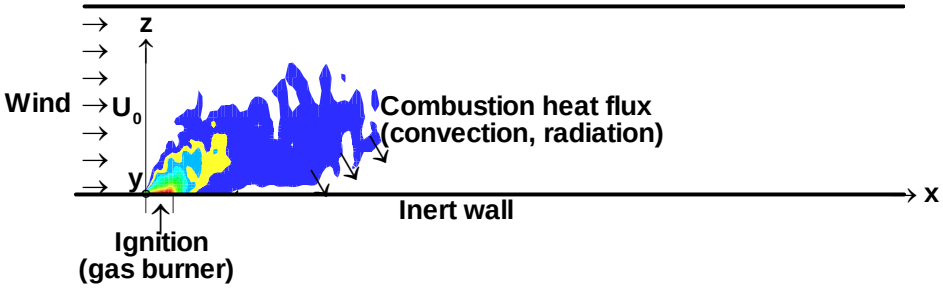

(a) Fire supplied by a gas burner

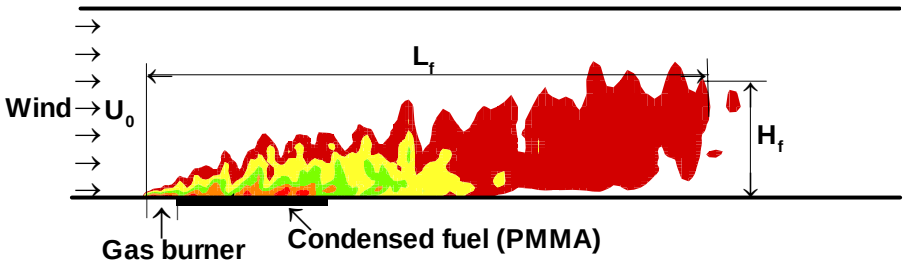

(b) Flame spread over surface of a condensed fuel

Fig. 2: Scheme of a flame spread over surface of a condensed fuel from a model calculation, and the coordinate system used in numerical simulation

In order to have a true predictive capability, it is important to understand what length scales must be resolved. For a fire plume, the characteristic length scale is related to the total heat release rate $\dot{Q}$ (kW) by the relation [10]:

$$L^* = \left(\frac{\dot{Q}}{\rho_\infty T_\infty c_p \sqrt{g}} \right)^{2/5} \text{(m)} \qquad (26)$$

In general, the large scale structure that is controlled by the inviscid terms can be completely described when this characteristic length L* is spanned by roughly ten computational cells. In this study, during flame spread, the heat release rate is higher than 100 kW, thus the characteristic length, L*, is in an order of 0.4 m. This implies that adequate resolution of the wall fire plume in large-scale can be achieved with a spatial resolution of about 4 cm. Moreover, in a LES calculation, commutation of the filtering operation with temporal and spatial differentiation is only strictly valid for uniform grid system. A compressed grid system contributes probably to the inaccuracies of a LES calculation. However, uniform grid system severely restricts its range of applicability to a small-scale fire in 3D simulation. Therefore, with the spatial reference value of 4 cm, the following factors are also considered for the particular wind-aided fire problem: (1) the computational nodes immediately adjacent to a solid wall are located in the fully turbulent region, sufficiently far away from the wall for viscous effects to be negligible ; (2) the grids are slightly stretched in the x and z directions and uniform in the y direction. With these considerations, the mildly stretched grid system, 150 (x) x 30 (y) x 40 (z), is used, offering the best tradeoff between accuracy and cost. In the x direction, start at 1.5 cm in the combustion zone, and stretch to about 6 cm at the free boundary. In the z direction, cell sizes are about 0.8 cm near the burning wall and stretch to about 2 cm far away from that region. Uniform grid of 1.3 cm is used in the transversal direction, y, of the channel. Using a DEC workstation, CPU times were of the order of 60 h for a real 300 s simulation from the ignition to the end of flame propagation over the PMMA surface.

In gas/solid combustion, the experiment duration is always too short to characterize the fire behaviour above the solid surface in a confined channel. Moreover, in order to protect the experimental set-up and instruments due to the strong flame radiation, the measurements during the flame propagation over the PMMA surface were not taken. During experiment, the heat feedback to the wall was measured by mounting the radiometers aperture of 150° view angle. Comparison to the experimental data is performed only from the fire with a heat release rate of 45 kW supplied by a gas burner with a length, $x_{b,}$ of 0.25 m following an inert wall downstream (Fig. 2a). Although, this tunnel experiment is 3D in nature, the reacting flow is essentially 2D in nature except in the flame tip region. Therefore, measurements for flame shape and heat flux were performed only on the median plane. The predicted and measured mean flame-surface heat flux downstream behind the burner ($x-x_b > 0$), along the burning wall centerline (y = 0.2 m) is presented in Fig. 3a & b. In spite of the discrepancy, the magnitude and distribution of the heat flux closely follow the general behavior of the experimental data in a range of wind velocity from 0.7 to 2.5 ms^{-1}. Just downstream behind the burner ($x-x_b < 0.25$ m), the total heat flux is found to decrease with an increase of the wind velocity due to reduction in the flame thickness. Far away from the burner ($x-x_b > 0.5$ m), the total heat flux, as a whole, is proportional to the wind velocity mainly due to an increase of the flame length. It should be noted that a cooling system for protecting the experimental set-up is not numerically simulated, and the different times for experiment (2 hours) and numerical simulation (60 s) are used for calculating the time-averaged values. Thus, rigorous comparison between prediction and measurement is again difficult for a large-scale fire spread. During experiment, a cooling water system was used to protect the wall material, and the buoyantly controlled flame produces oscillatory behaviour in flame structure in cyclic fashion, both yielding the measurement error with an uncertainty of 10 to 15%. In the numerical simulation, the Smagorinsky sub-grid model is known as being too dissipative, particularly for the stretched grid system. It seems most likely that the difference between the prediction and measurement is due to a combination of experimental uncertainties and the possibility error in the numerical simulation.

As the PMMA is introduced downstream the burner (Fig. 2b), the flame spread occurs as a result of heating of the unignited part of the fuel surface to an ignition temperature of 380°C at which the pyrolysis flux exceeds a certain threshold level. The predicted radiative and convective heat fluxes with the pyrolysis front, during the fire propagation, from the flame to the surface of condensed fuel along the wall centerline (y = 0.2 m) are plotted in Figs. 4 and 5 for different wind velocities. As buoyancy controls the flame thickness, the radiative heat fluxes (cf. Fig. 4) suggest an inverse dependence with the wind velocity U_0. A monotonous decrease of the maximum radiation flux from 60 to 40 kWm^{-2} is brought about due to reduction in the flame thickness with an increase of the wind velocity from 0.5 to 2.5 ms^{-1}. The convective heat flux (cf. Fig. 5) appears insensitive to the wind velocity lower than 1.5 ms^{-1}, and however, increases significantly for a further

increase of the wind velocity to 2 ms^{-1}. The value of the mean convection flux is found to increase from 12 to 18 kWm^{-2} with an increase of the wind velocity due to enhancement of the turbulence level and reduction in the flame stand-off distance. With an increase of the wind velocity, reduction in the flame-surface radiation flux is momentarily compensated by an increase of the convection flux, resulting in a total heat flux practically independent to the wind velocity. Also plotted in Fig. 6 is the radiative fraction of the total flame-surface heat flux. The predicted results suggest the dominance of radiative heat flux, which is higher than 70% of the total heat flux, during the flame propagation over the surface of a condensed fuel in large scale along the channel.

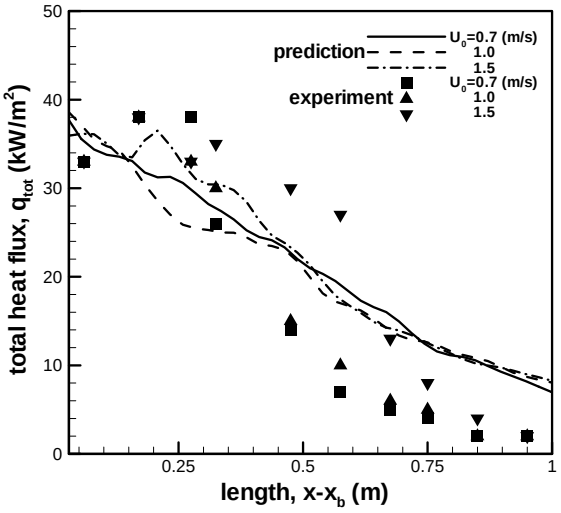

(a) Heat flux for U_0 = 0.7, 1 and 1.5 ms^{-1}

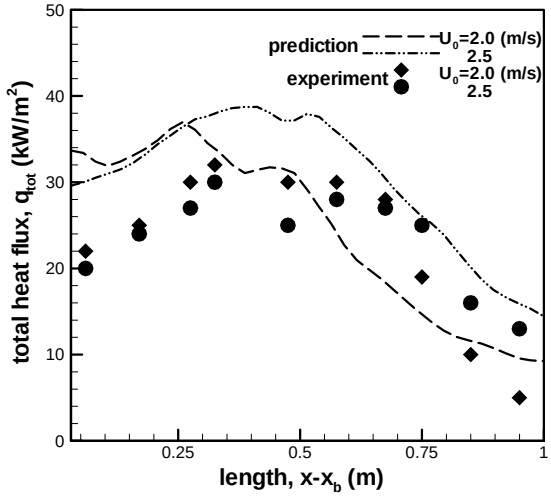

(b) Heat flux for U_0 = 2 and 2.5 ms^{-1}

Fig. 3: Comparison between predicted and measured total heat flux from the flame to the wall surface downstream behind the burner

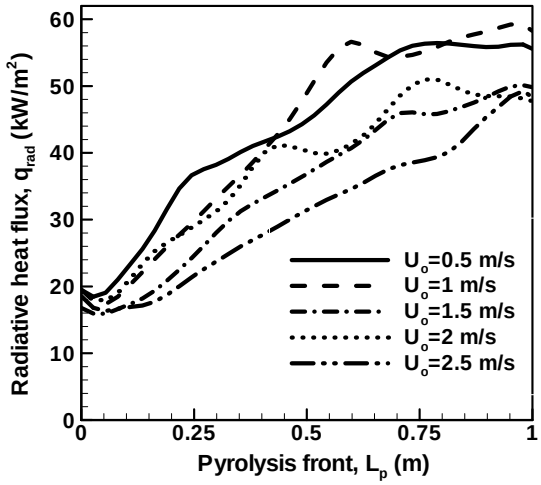

Fig. 4: Predicted radiation flux with the pyrolysis front for different wind velocities

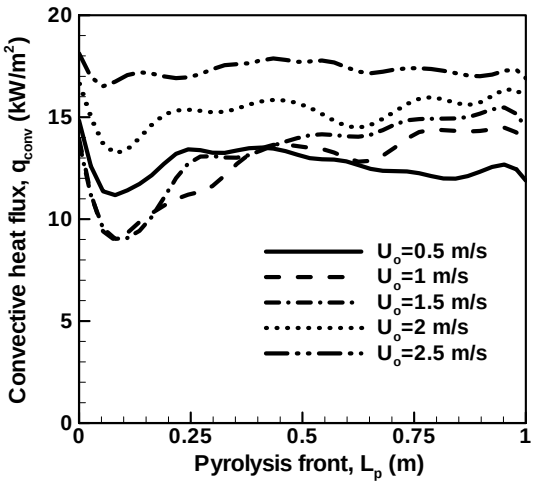

Fig. 5: Predicted convection flux with the pyrolysis front for different wind velocities

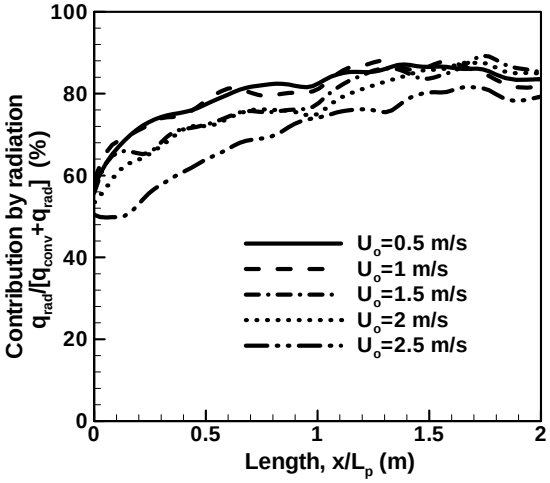

Fig. 6: Contribution by flame radiation to the total heat flux with the pyrolysis front for different wind velocities

During the fire propagation, the flame shape (length/height) is strongly controlled by the distributions of the existing oxygen mass fraction inside the channel, as shown in Fig. 7a & b. For the wind velocity of 0.5 ms^{-1} (cf. Fig. 7a), before the flame propagation over the fuel surface, the oxygen mass fraction is sufficiently high to consume all the fuel inside the channel, and we have a fuel-controlled fire. However, during the flame spread (cf. Fig. 2b), the available oxygen mass fraction after the combustion inside the channel decreases rapidly up to 8%. As a consequence, the excess fuel from the pyrolysis zone has to be burned downstream far away from the pyrolysis zone where the oxygen is still available, and therefore, we have a ventilation-controlled fire. While for the wind velocity of 2.5 ms^{-1} (cf. Fig. 7b), the oxygen mass fraction is always sufficiently high to consume all the fuel inside the channel, and we have a fuel-controlled fire. The flame shape, characterized by the flame height, H_f, and length, L_f, as defined in Fig. 2b, is compared to the experimental data from a gas burner fire (45 kW) under the condition of fuel-controlled fire. In the experiment, a maping flame luminosity technique [3] using a CCD camera was developed to measure the visible flame shape through images processing using a selected luminosity threshold. This technique is based on the flame presence probability, and the mean flame length/height are derived from the maximum flame ones corresponding to the presence probability of 0.05 and the continuous ones corresponding to the presence probability of 0.95. It was checked that the so-determined persistent flame regime corresponds to a gas temperature of about 450 to 500 °C. By using this criterion for the mean flame shape, the predicted mean flame height/length are compared with the experimentally-determined ones in Fig. 8 for the different wind velocities. Both the experiment and prediction show that the flame length progressively increases, and however, the flame height decreases with an increase of the wind velocity. As compared to the experimentally-determined flame length, an overprediction of 10% for $U_0 = 0.5$ ms^{-1}, and a underprediction of 20% for $U_0 = 1.5$ ms^{-1} are found. Evolution of the flame height with the wind velocity is correctly predicted. The flame shape (length/height) on the median plane as a function of the pyrolysis front during the flame propagation over the PMMA surface for the wind speeds between 0.5 and 2.5 ms^{-1}, is shown in Fig. 9a & b. The flame propagation over condensed fuel surface occurs in two successive modes. In the first mode ($x/L_p < 0.3$), when the flame is confined within a boundary layer, the flame is progressively elongated in the downstream direction with a flame shape practically independent of the wind velocity. Transition to the second mode, occurring earlier at low wind velocity ($U_0 < 1.5$ ms^{-1}) where the flame stands up to form a buoyant plume. The second mode is evident from a sharp rise of the flame height (cf Fig. 9b) in the slope of the curves, and seen to occur at $x/L_p \approx 0.3$ where the ratio (Froude number) of the horizontal and the upward forces in the flow stream is low. However, for the fuel controlled fire ($U_0 > 1.5$ ms^{-1}), the flame height becomes independent of the wind speed. The flame at low wind velocity is roughly six times thicker than that at high wind velocity mainly due to buoyancy and air entrainment. The extent of the visible flame, L_f, is about 4 times the pyrolysis length, L_p, for a ventilation-controlled fire ($U_0 < 1.5$ ms^{-1}), and reachs an asymptotic value of 2 times the pyrolysis length for the wind velocity higher than 2 ms^{-1}. Globally, the extent of the visible flame, L_f, for a ventilation-controlled fire is about 2 times that for fuel-controlled fire.

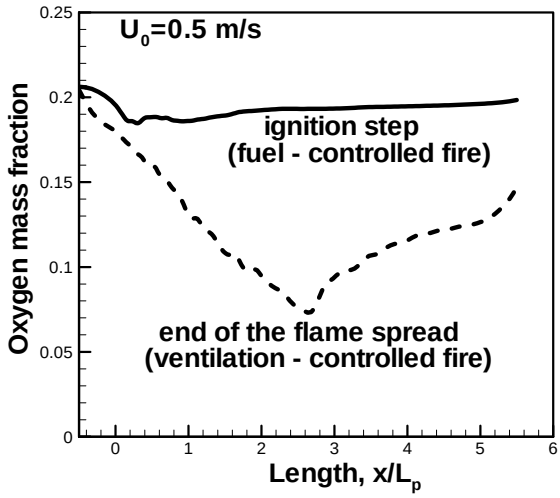

(a) $U_0 = 0.5$ ms^{-1}

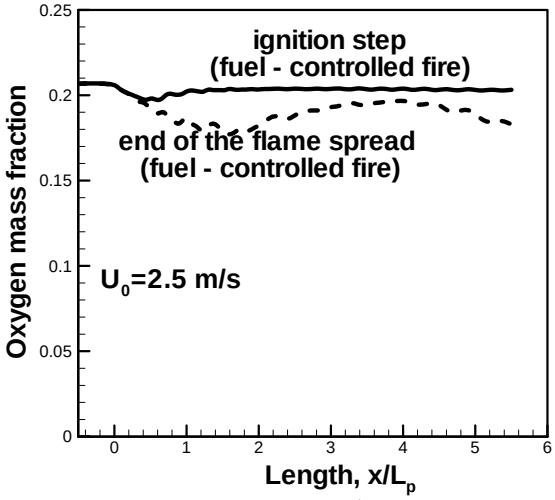

(b) $U_0 = 2.5$ ms^{-1}

Fig. 7: Evolution of the predicted oxygen mass fraction along the channel with the pyrolysis front

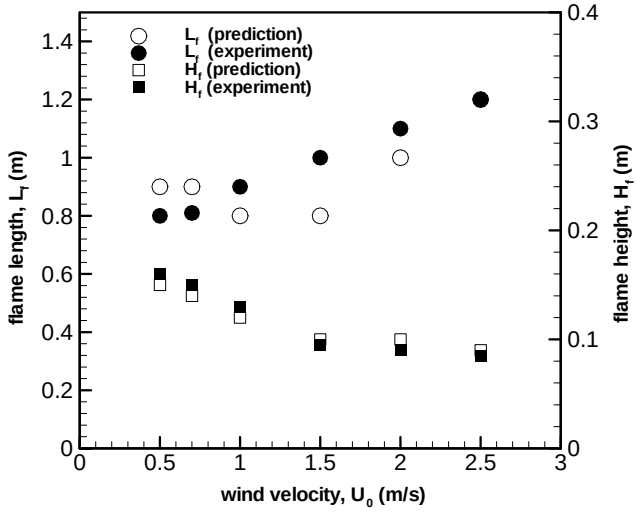

Fig. 8: Comparison between the predicted and measured flame height/length as a function of the wind velocity

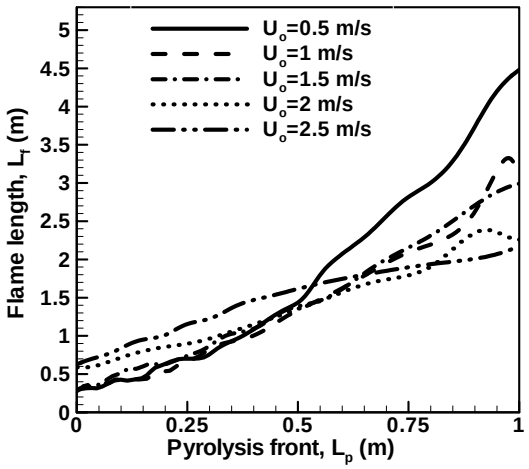

(a) Flame length

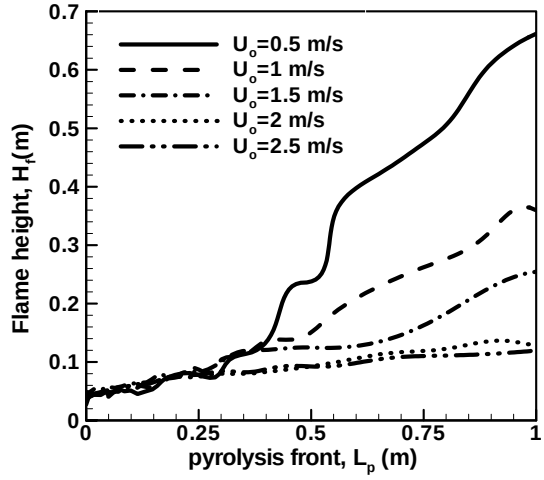

(b) Flame height

Fig. 9: Predicted flame shape as a function of the pyrolysis front for the different wind velocities

An expression for the flame spread velocity, defined as the pyrolysis front advancement rate, is derived from the following expression, $V_f = dx_p/dt$. The time for the temperature at a given position over PMMA surface to reach the ignition temperature of 380°C is selected for the pyrolysis front arrival time, dt, for calculating the pyrolysis spread rate. Here, we have ignored the transient effects due to conduction loss in the thermally thin PMMA sheet. Evolution of the flame spread velocity as a function of the pyrolysis front for different wind speeds is shown in Fig. 10. The overall flame spread process can be divided into two modes. For the first boundary layer mode ($x/L_p < 0.25$), V_f is essentially constant with the pyrolysis front, and generally higher for high wind velocity. Transition to the second plume mode far away from the inlet zone, a quick increase of V_f occurs with the pyrolysis front up to reaching an asympotic value of 3 ± 0.5 cms^{-1}. That means that solid fuel fires in a confined channel have flame spread rates controlled by heat transferred through both convection and radiation from the turbulent flame to the unburnt fuel surface. Since the total heat flux (cf. Figs. 4 and 5) is practically independent to the wind velocity, V_f is essentially independent of air cross-flow. The predicted maximum flame spread velocity consists with the measured one over PMMA surface [7,8]. Fig. 11 shows variations of the spatial average fuel mass loss (pyrolysis) flux, $\dot{m}_s$, along the pyrolysis front, L_p, at different wind speeds between 0.5 and 2.5 ms^{-1}. It is seen that $\dot{m}_s$ increases quickly as the fire propagates up to $x/L_p < 0.4$ and is generally higher at lower wind velocity due to the stronger radiation flux. Beyond the zone for $x/L_p > 0.4$, the fuel pyrolysis rate reaches an asymptotic value of approximately 28 gm^{-2}s^{-1}, independent of the wind speed due to the constant total heat flux.

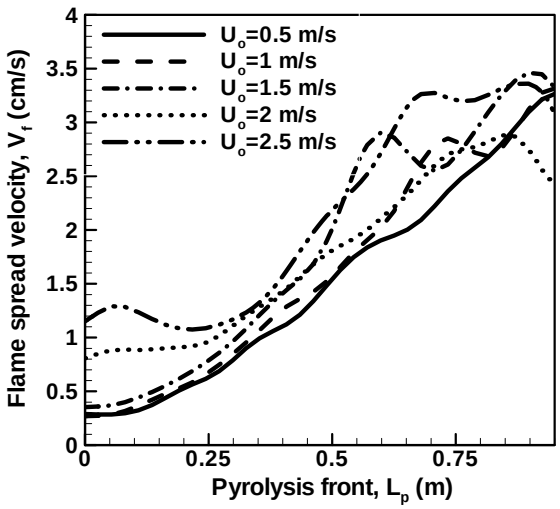

Fig. 10: Predicted flame spread rate with the pyrolysis front for the different wind speeds

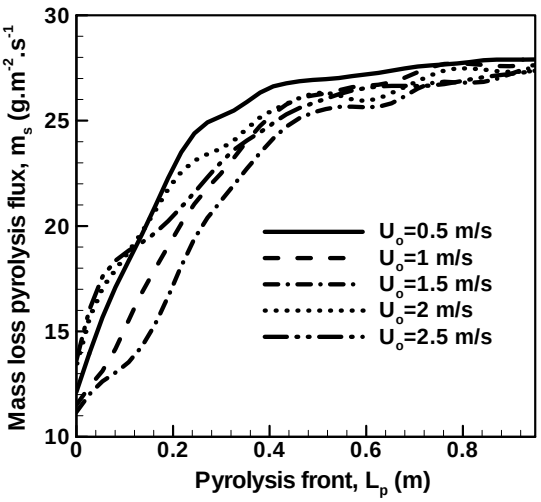

Fig. 11: Predicted mass loss flux with the pyrolysis front for the different wind speeds

The predicted profiles of the normalized mean axial velocity, u/U_0, at two locations (x/L_p = 1 and 4.5) for the wind velocity varying from 0.5 to 2.5 ms^{-1} are plotted in Fig. 12 a & b. The velocity profiles are strongly influenced by the ventilation conditions. For the low wind velocity of 0.5 ms^{-1}, the fire acts as a thermal blockage, the magnitude of the buoyancy and inertia forces is almost identical, resulting in a strong acceleration of the air stream as it approaches the fire due to the combined effects of natural convection and air entrainment. Along the channel, acceleration of air flow results in a significant increase of the wind velocity from 5 times at the end of condensed fuel (x/L_p = 1), to 8 times at the exit (x/L_p = 4.5) of the channel from the original magnitude. Moreover, for the U_0 = 0.5 ms^{-1}, the maximum velocity occurs in the reacting boundary layer at x/L_p = 1 due to the dominant inertia force, and moves towards the ceiling at x/L_p = 4.5 due to a significant flame stand-off distance forming a buoyant plume. However, for the wind velocity higher than 1.5 ms^{-1}, the flow is dominated by the inertia force, and the profiles of the axial velocity are rather similar with an acceleration of air flow to about 2 times from the original magnitude all along the channel due to turbulence development. The predicted profiles of the mean temperature at the two stations (x/L_p = 1 and 4.5) along the channel for different wind speeds are presented in Fig. 13 a & b. At the end of the condensed fuel (x/L_p = 1), the maximum temperature for the different wind velocities is almost identical in the reacting region. Near the ceiling, the high wind speed results in a significant decrease of temperature level. For the wind velocity lower than 1 ms^{-1}, the buoyant plume is detached to the horizontal wall at the exit of the channel (x/L_p = 4.5), and capable of reaching the ceiling, causing a significant temperature stratification. However, for the wind velocity higher than 1 ms^{-1}, the profiles of the mean temperature at the exit of the channel (x/L_p = 4.5) are practically uniform, and the temperature level decreases with an increase of the wind speed.

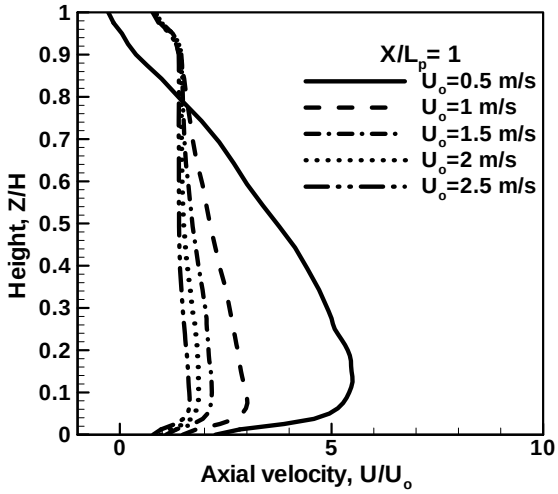

(a) At x/L_p = 1

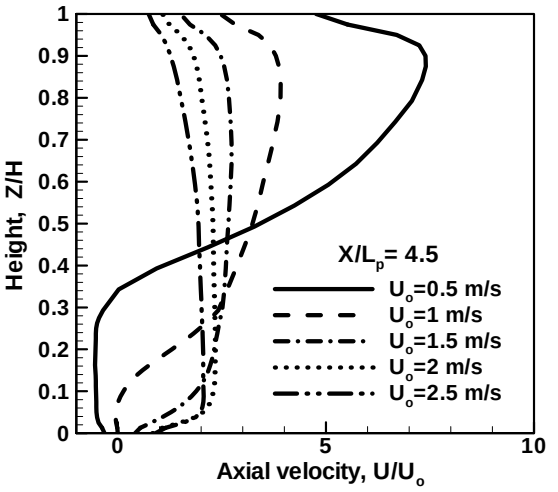

(b) At x/L_p = 4.5

Fig. 12: Predicted profiles of the normalized mean axial velocity, u/U_0, as a function of the wind velocity

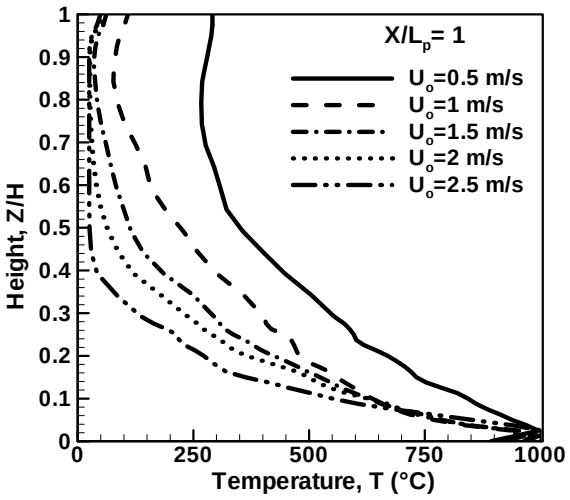

(a) At $x/L_p = 1$

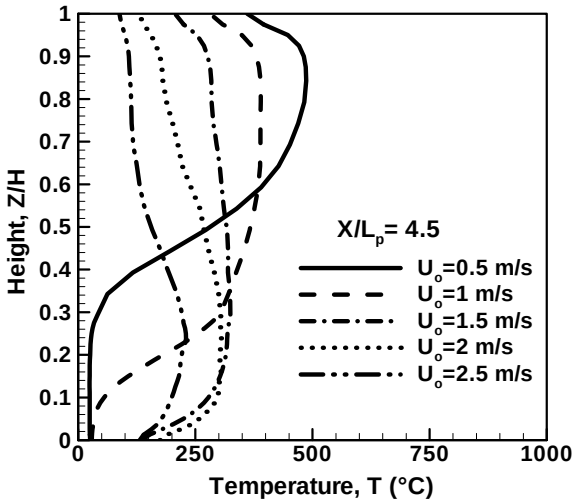

(b) At $x/L_p = 4.5$

Fig. 13: Predicted profiles of the mean temperature as a function of the wind velocity

4. CONCLUSION

Large Eddy Simulation is used for modeling the wind-aided flame propagation over a condensed fuel surface in a confined tunnel. Globally, the predicted mean flame shape (height/length) and heat flux are in relatively good agreement with the experimental data from a burner fire in an intermediate scale model channel. The behavior of the large-scale, highly transient flame spread over noncharring solid fuel surface are also reasonably well reproduced. An analysis of the predicted results in light of the fluid flow, heat transfer and flame spread gives an insight into some of the mechanisms governing the wind-blown fire spread and burning. The wind-aided flame propagation over condensed fuel surface occurs in two successive modes. In the boundary layer mode, the flame height and length are practically independent of the wind speed. Transition to the buoyancy controlled plume mode, happening sooner under ventilation controlled fire ($U_0 < 1.5$ ms^{-1}), the flame height and length increases significantly with a decrease of the wind speed. The flame length is found to be roughly 2 times the pyrolysis length for fuel controlled fire, and 4 times one for ventilation controlled fire. An increase of the wind velocity results in an increase of the convection flux, and however, a decrease of the radiation flux. Consequently, the total heat flux from the flame to the surface of condensed fuel is practically independent of the wind velocity. In all the cases, contribution by radiation for the flame propagation is higher than 70% of the total heat flux. The fire spreads slowly in a boundary layer mode, and later, the flame tends to tilte from the horizontal wall, accompanied by a strong acceleration of the flame spread. The prediction shows that the maximum flame spread rate of 3 ± 0.5 cms^{-1} and pyrolyse rate of 28 gm^{-2}s^{-1} for PMMA are practically independent of air flow velocity due to the identical total heat flux.

The future work introduces the more descriptions of the condensed fuel pyrolysis chemistry. Ongoing work is accounting for a dynamic subgrid-scale model for the wind-aided flame spread in a channel.

NOMENCLATURE

A_0	constant in soot model
C_{Ebu}	constant in EBU model
c_p	specific heat of the gas
c_s	specific heat of the solid or soot concentration
C_s	Smagorinsky constant
C_μ,C_ε	empirical constants in turbulence model
d_p	diameter of soot particle
E	surface roughness or energy activation of the soot
f-g	constant in soot model
f_v	soot volume fraction
g_0	coefficient of linear termination on soot particle
g_i	acceleration of gravity in the co-ordinate directions x, y and z
h	enthalpy
h_g	heat of vaporization
H	height of the channel
H_o	heat release rate per unit mass of oxygen consumed
I	radiative intensity
I^l	radiative intensity for a single ordinate direction, l
k	turbulent kinetic energy
L	length of the channel
L^*	characteristic length scale of the fire
m_p	mass of a soot particle

$\dot{m}_s$	local burning rate per unit area
n	unit normal vector
N	soot number density
p	pressure
P	empirical function of Jayetilleke
Pr	laminar Prandtl number
Pr_t	turbulent Prandtl number
$\dot{q}_c'''$	heat release rate per unit volume
$\dot{q}_{conv}$	convective heat feedback to the solid surface
$\dot{q}_{pyro}$	energy available for pyrolyzing the condensed fuel
q_r	radiant energy flux
$\dot{q}_{rad}$	radiation from flame to the solid surface
$\dot{Q}$	total heat release
R	universal gas constant
S_{ij}	local large scale rate of strain
Sc_t	turbulent Schmidt number
t	time
T	temperature
T_g	gas temperature near the wall surface
T_w	wall surface temperature
T_s	solid temperature
T_∞	ambient temperature
u_i , u_j	velocity components in the co-ordinate directions x, y and z
w^l	weighting factor in the discrete ordinates method
x	streamwise coordinate
x_b	length of the burner
x_i, x_j	co-ordinate directions x, y and z
y	cross-stream coordinate
y^+	wall coordinate
Y_i	mass fraction of the specie, i
Z	mixture fraction
Z_{st}	stoichiometric mixture fraction

Greek Symbols

ε	dissipation of the turbulent kinetic energy
ε_w	emissivity of the solid surface
μ_t	turbulent viscosity
ν_s	stoichiometric oxygen requirement to burn 1kg soot
ν_F	stoichiometric oxygen requirement to burn 1kg fuel
ρ	density
ρ_s	density of the solid material
ρ_∞	ambient density
δ	thickness of the solid material
α, β	constants in soot model
Δ	filter width
σ	Stefan-Boltzmann constant
ϕ	general variable
$\overline{\varphi}$	resolvable-scale component
φ'	subgrid-scale component
$\dot{\omega}_o$	oxygen consumption rate
$\dot{\omega}_{Oxid}$	soot oxidation rate
Ω	domain of the radiation propagation
$\vec{\Omega}$	direction of the radiation propagation
Ω'	incoming direction of radiation
$\tau_{ij,SGS}$	subgrid scale Reynolds stress tensor
κ	total absorption coefficient or von Karman constant

Overbar

-	filtered variable

REFERENCES

1. M. Lavid and A.L. Berlad, “Gravitational effects on chemically reacting boundary layer flows over a horizontal flat plate”, Sixteenth Symposium (International) on Combustion. Pittsburgh, The Combustion Institute, pp. 1157-1164 (1976).
2. A.A. Putnam, “A model study of wind-blown free burning fires”, Tenth Symposium (International) on Combustion, Pittsburgh, The Combustion Institute, pp. 1039-1046 (1963).
3. G. Kolb, J.L. Torero, J.M. Most and P. Joulain, “Cross flow effects on the flame height of an intermediate scale diffusion flame”, Proceedings of the International Symposium on Fire and Technology, Seoul, Korea, pp. 169-177 (1997).
4. Y. Wu and M.Z.A. Bakar, “Control of smoke flow in tunnel fires using longitudinal ventilation systems – a study of the critical velocity”, Fire Safety Journal, Vol. 35, pp. 363-390 (2000).
5. D.F. Fletcher, J.H. Kent, V.B. Apte and A.R. Green, “Numerical simulations of smoke movement from a pool fire in a ventilated tunnel”, Fire Safety Journal, Vol. 23, pp. 305-325 (1994).
6. P.J. Woodburn and R.E. Britter, “CFD simulation of a tunnel fire – Part I”, Fire Safety Journal, Vol. 26, pp. 35-62 (1996).
7. V.B. Apte, R.W. Bilger, A.R. Green and J.G Quintiere, “Wind-aided turbulent flame spread and burning over large-scale horizontal PMMA surfaces”, Combustion and Flame, Vol. 85, pp. 169-184 (1991).
8. J.P. Frank and P.L. Charles, Flame spread over horizontal surfaces of polymethylmethacrylate, Twenty-Fourth Symposium (International) on Combustion, Pittsburgh, The Combustion Institute, pp. 1661-1668 (1992).
9. L. Zhou and A.C. Fernandez-Pello, “Solid fuel combustion in a forced, turbulent, flat plate flow: the effect of buoyancy”, Twenty-Fourth Symposium (International) on Combustion, Pittsburgh, The Combustion Institute, pp. 1721-1728 (1992).

10. K.B. McGrattan, P.F. Glenn and E.F. Jason, Fire Dynamics Simulator – Technical Reference Guide, NIST Technical Report (2007).

11. J. Smagorinsky, “General circulation experiments with the primitive equations I. The basic experiment”, Monthly Weather Review, Vol. 91, No. 3, pp. 99-164 (1963).

12. C. Huggett, “Estimation of the rate of heat release by means of oxygen consumption measurements”, Fire and Materials, Vol. 4, No. 2, pp. 61-65 (1980).

13. P.A. Tesner, T.D. Snegiriova and V.G. Knorre, “Kinetics of dispersed carbon formation”, Combustion and Flame, Vol. 17, pp. 253-260 (1971).

14. J.B. Moss, C.D. Stewart and K.J. Young, “Modelling soot formation and burnout in a high temperature laminar diffusion flame burning under oxygen-enriched conditions”, Combustion and Flame, Vol. 101, pp. 491-500 (1995).

15. H.Y. Wang and P. Joulain, “Modeling on burning of large-scale vertical parallel surfaces with fire-induced flow”, Fire Safety Journal, Vol. 32, pp. 241-271 (1999).

16. A.T. Modak, “Radiation from products of combustion”, Fire Research, Vol. 1, pp. 339-360 (1979).

17. N. Djilali, I. Gartshore and M. Salcudean, “Calculation of convective heat transfer in recirculating turbulent flow using various near-wall turbulence models”, Numerical Heat Transfer, Vol. 16, pp. 189-212 (1989).

18. J.G. Quintiere, Principles of fire behavior, Delmar Publishers, Albany, New York (1998).